SEISMIC MONITORING OF CO_2 INJECTION USING A DISTORTED BORN T-MATRIX APPROACH IN ACOUSTIC APPROXIMATION

KENNETH MUHUMUZA[1], MORTEN JAKOBSEN[2], TEEMU LUOSTARI[1] and TIMO LÄHIVAARA[1]

[1]*Department of Applied Physics, University of Eastern Finland, Kuopio, Finland. kenneth.muhumuza@uef.fi*
[2]*Department of Earth Sciences, University of Bergen, Bergen, Norway.*

(Received September 17, 2017; revised version accepted July 2, 2018)

ABSTRACT

Muhumuza, K., Jakobsen, M., Luostari, T. and Lähivaara, T., 2018. Seismic monitoring of CO_2 injection using a distorted Born T-matrix approach in acoustic approximation. *Journal of Seismic Exploration*, 27: 403-431.

Monitoring the injected CO_2 distribution is at the core of any carbon capture and storage project. Waveform inversion methods can be used to obtain high-resolution images for monitoring the injected CO_2 in the subsurface, but remains computationally challenging. Efficient modelling approximations are desirable for solving time-lapse inversion problems and to test the settings in which they give accurate predictions. We employed the distorted Born approximation (based on scattering integral equation) to simulate time-lapse synthetic data for a CO_2 injection scenario with a single injector, and benchmarked it against the finite element and exact T-matrix approach. The distorted Born approximation presented, considers a general heterogeneous reference medium; and provides a framework for imaging of regions of time-lapse variation using the baseline survey as a reference and the monitor survey as perturbed to directly estimate the perturbation.

Based on our simplified velocity model of CO_2 injection, synthetic testing demonstrated that the new distorted Born approximation provides accurate predictions of the difference data seismograms. We tested the distorted Born iterative T-matrix (DBIT) inversion method on a synthetic dataset generated using T-matrix forward modelling, and

0963-0651/18/$5.00

we investigated three inversion approaches. The inversion results showed that the DBIT method sufficiently retrieves the time-lapse velocity changes even in the cases of relatively low signal-to-noise ratio. The inversion approach that focused on the time-lapse data variation (perturbation only) gave improved results in noisy and noise free environments. We also applied DBIT inversion to a synthetic dataset generated using the finite element method, in order to avoid inverse crimes. The inversion recovered the trend of the velocity models, but with some inaccuracies in the estimates for the time-lapse velocity changes. The DBIT method which considers a dynamic background media and T-matrix approach may be a potential tool in seismic characterisation of subsurface reservoirs and efficient for monitoring of CO_2 sequestration.

KEY WORDS: waveform inversion, inverse theory, time-lapse seismic, scattering theory, wave propagation, computational seismology, CO_2 sequestration.

INTRODUCTION

The geological storage of carbon dioxide (CO_2) is a promising strategy that can contribute to climate mitigation efforts (IPCC, 2014). The success of the strategy relies on the ability to securely isolate the stored CO_2 from oceans and the atmosphere. For this purpose, monitoring the injected CO_2 distribution is at the core of any carbon capture and storage (CCS) project. Seismic methods have proven useful in monitoring the migration and accumulation of the injected CO_2 in the subsurface (Shi et al., 2007; White et al., 2011; Chadwick et al., 2009; Couëslan et al., 2014; Ivandic et al., 2015; Pevzner et al., 2017). These methods are based on the fact that injection of CO_2 into subsurface structures change their elastic properties, which in turn influence seismic wave propagation.

A common observation resulting from the injection process is an increase in reservoir pressure and a decrease in P-wave velocity of the reservoir formation (Carcione et al., 2006; Shi et al., 2007; Marston, 2013). Among the seismic monitoring methods, full waveform inversion (FWI) has received considerable attention for its advantage to properly map changes in CO_2 distribution (Zhang et al., 2013; Romdhane and Querendez, 2014; Zhang et al., 2016). The FWI approach is preferred over other conventional seismic monitoring methods such as travel-time inversion and pre-stack Kirchhoff migration (Raknes et al., 2015; Kasahara and Hasada, 2016), because the FWI scheme can predict desired velocity changes from seismic data; providing more accurate estimates of CO_2 saturation changes in the reservoir.

In principle, FWI is a non-linear data fitting procedure that aims at obtaining detailed estimates of subsurface properties from seismic data, by minimising the misfit between the observed and predicted data. It can be performed in the time-space domain (Tarantola, 1984; Sheen et al., 2006; Lähivaara et al., 2015) or in the frequency-space domain (Pratt, 1999; Jakobsen and Ursin, 2015). The frequency domain is considered less

computationally expensive, especially when relatively fewer frequencies are used to obtain accurate inversion results. This can be achieved by strategically selecting the frequencies used in the inversion (Sirgue and Pratt, 2004; Kim et al., 2011); finding a compromise between accuracy and computational cost.

Most successful applications of FWI for CO_2 monitoring on both synthetic and real seismic data, are implemented with gradient-based local optimisation methods, or rather, more compute-intensive Newton-based methods (Zhang et al., 2013; Queißer and Singh, 2013; Raknes et al., 2013; Zhang et al., 2016). Current research efforts within FWI strive to reduce the computational cost by developing efficient approaches and testing the settings in which they give accurate predictions. One such approach is using scattering-integral-based methods (Haffinger et al., 2013; Jakobsen and Ursin, 2015). In relation to time-lapse imaging, the scattering theory provides a framework for imaging of regions of time-lapse variation using the baseline survey as a reference and the monitor survey as perturbed to directly estimate the perturbation (see Zhang, 2006; Innanen et al., 2014).

In this paper, we apply newly developed non-linear direct iterative T-matrix method based on the distorted Born approximation (DBIT) (Jakobsen and Ursin, 2015), for time-lapse seismic monitoring of CO_2 injection. We do this by generating synthetic data over layered media, before and after CO_2 injection. The target layer in the injection area is a few tens of meters deep. Shallow CO_2 injection depths ($<$1000 m) are typical for many test sites (e.g., Gritto et al., 2004; Zhang et al., 2013; Nowroozi et al., 2016), where the objective is to have a controlled injection experiment to monitor migration and behaviour of gas plume. Our aim is to investigate the feasibility and efficiency of the DBIT, a new variant of distorted Born iterative methods, for solving time-lapse inversion problems. Contrary to adjoint-based FWI methods (Virieux and Operto, 2009; Liao, 2015), the DBIT method employs the use of Green's functions to explicitly formulate the sensitivity matrix.

The recent proven success of waveform inversion applications in time-lapse problems has led to the development of different time-lapse data inversion approaches. These approaches that include parallel difference, sequential difference, and double-difference have been discussed in relation to FWI (Raknes et al., 2013; Zhang and Huang, 2013; Maharramov and Biondi, 2014; Asnaashari et al., 2015) and linearized waveform inversion (Ayeni et al., 2011).

Based on the aforementioned research, we investigate the feasibility of three inversion approaches for our synthetic data. In the first approach, the different seismic waveform data corresponding to baseline and monitor survey are inverted separately. We utilise the same starting model for the two separate inversions, then the difference between the inverted baseline

and inverted monitor models correspond to the time-lapse variation. In the second approach, we supply the inverted baseline model as the starting model for the monitor inversion known as the sequential difference (Asnaashari et al., 2015). This approach may be advantageous in that it is not affected too much by repeatability issues of the two acquisition surveys (baseline and monitor), and converges faster; however, artefacts may arise since the starting models are not consistent (Raknes et al., 2013). In the third approach, we apply double-difference waveform inversion (Raknes et al., 2013; Zhang and Huang, 2013; Asnaashari et al., 2015), which is equivalent to inverting the time-lapse data variation (pertubation) only. Finally, we study the effects of noise to test which approach may maintain relatively low levels of image artefacts and provide accurate quantitative estimates of time-lapse velocity changes. Adding noise not only validates the stability but also makes the numerical experiments more realistic.

METHODOLOGY

The forward problem and distorted Born approximation

In many seismic experiments, modelling of reflection seismic data is achieved by assuming that the subsurface structure behave acoustically in order to simplify the algorithms and reduce the computational burden (Prieux et al., 2009; Ayeni and Biondi, 2010; Zhang et al., 2013; Romdhane and Querendez, 2014; Jakobsen and Ursin, 2015). In the acoustic approximation, only P-waves are modelled. If the density is constant in a region of domain Ω_{tot}, the acoustic pressure field $p(\mathbf{x},\mathbf{x}_s,\omega)$ due to a source $f_s(\mathbf{x}_s,\omega)$ at position $\mathbf{x}_s$ is governed by the Helmholtz equation:

$$\left[\nabla^2+\frac{\omega^2}{c^2(\mathbf{x})}\right]p(\mathbf{x},\mathbf{x}_s,\omega)=-\delta(\mathbf{x}-\mathbf{x}_s)f_s(\mathbf{x}_s,\omega),\qquad \mathbf{x},\mathbf{x}_s\in\Omega_{\text{tot}}\ , \tag{1}$$

where $c(\mathbf{x})$ is the acoustic wave velocity as a function of position, ω is the angular frequency, and δ is the Dirac's delta function.

We can separate the velocity model $c(\mathbf{x})$ into a slowly varying background model $c^{(0)}(\mathbf{x})$ and a perturbation model $m(\mathbf{x})$

$$m(\mathbf{x})=\left(\frac{\left[c^{(0)}(\mathbf{x})\right]^2}{\left[c(\mathbf{x})\right]^2}-1\right)\ . \tag{2}$$

For a finite range perturbation $m(\mathbf{x})$, the Lippmann-Schwinger equation (e.g., Cohen and Bleistein, 1977; Ikelle and Amundsen, 2005; Colton and Kress, 2012) corresponding to eq. (1) can be expressed as

$$p(\mathbf{x},\mathbf{x}_s,\omega) = p^{(0)}(\mathbf{x},\mathbf{x}_s,\omega) + k_0^2 \int G^{(0)}(\mathbf{x},\mathbf{x}',\omega) m(\mathbf{x}') p(\mathbf{x}',\mathbf{x}_s,\omega) \mathrm{d}\mathbf{x}' \quad , \tag{3}$$

where $p(\mathbf{x},\mathbf{x}_s,\omega)$ is the outgoing wavefield, $k_0 = \omega / c^{(0)}$ is the wave number and $p^{(0)}(\mathbf{x},\mathbf{x}_s,\omega)$ is the incident wavefield for the known Green's function $G^{(0)}(\mathbf{x},\mathbf{x}_s,\omega)$ of the background model, expressed as

$$p^{(0)}(\mathbf{x},\mathbf{x}_s,\omega) = G^{(0)}(\mathbf{x},\mathbf{x}_s,\omega) f_s(\omega) \quad . \tag{4}$$

The causal Green's function $G^{(0)}(\mathbf{x},\mathbf{x}',\omega)$ in eq. (3) is the wavefield at point $\mathbf{x}$ due to a point source at $\mathbf{x}'$ in the background model and is a solution of the following equation

$$\left[\nabla^2 + k^2\right] G^{(0)}(\mathbf{x},\mathbf{x}',\omega) = -\delta(\mathbf{x}-\mathbf{x}') \quad . \tag{5}$$

If the background model is homogeneous, explicit analytical solution of $p^{(0)}(\mathbf{x},\mathbf{x}',\omega)$ can be obtained; and the first-order Born approximation consists of replacing the total pressure wavefield by the incident wavefield. For inhomogeneous background models, characterised by a wave number that varies with position, the approximate Green's function can be computed using ray theory (e.g., Thierry et al., 1998; Cerveny, 2005; Moser, 2012), if the model is a smoothly varying media with smooth interfaces. However, for any general heterogeneous background medium appropriate numerical methods such as the T-matrix (Jakobsen, 2012) and finite difference (Kirchner and Shapiro, 2001) can be used to compute the Green's functions in the background model. In our work, we generate approximate Green's function for a heterogeneous background medium using distorted Born approximation (DBA) based on the theory in Jakobsen and Ursin (2015). The theory establishes a connection between the Green's functions $G(\mathbf{x},\mathbf{x}')$ and $G^{(0)}(\mathbf{x},\mathbf{x}')$ for the heterogeneous and homogeneous background media respectively through the so-called Dyson equation (Jakobsen and Ursin, 2015)

$$G(\mathbf{x},\mathbf{x}') = G^{(0)}(\mathbf{x},\mathbf{x}') + k_0^2 \int_\Omega G^{(0)}(\mathbf{x},\mathbf{x}'') m(\mathbf{x}'') G(\mathbf{x}'',\mathbf{x}) \mathrm{d}\mathbf{x}'' \quad , \tag{6}$$

where Ω denotes the domain where the scattering potential is non-zero.

We can rewrite the Lippmann-Schwinger and Dyson eqs. (3) and (6) for the total wavefield in the form of a product of matrices for ease in discretization (Jakobsen and Ursin, 2015) such that

$$p(\mathbf{x}) = p^{(0)}(\mathbf{x}) + \int_{\Omega} \mathrm{d}\mathbf{x}_1 \int_{\Omega} \bar{G}^{(0)}(\mathbf{x}, \mathbf{x}_1) \tilde{V}(\mathbf{x}_1, \mathbf{x}_2)\, p(\mathbf{x}_2) \mathrm{d}\mathbf{x}_2 , \quad (7)$$

$$\bar{G}(\mathbf{x}, \mathbf{x}') = \bar{G}^{(0)}(\mathbf{x}, \mathbf{x}') + \int_{\Omega} \mathrm{d}\mathbf{x}_1 \int_{\Omega} \bar{G}^{(0)}(\mathbf{x}, \mathbf{x}_1) \tilde{V}(\mathbf{x}_1, \mathbf{x}_2) \bar{G}(\mathbf{x}_2, \mathbf{x}') \mathrm{d}\mathbf{x}_2 , \quad (8)$$

where $\tilde{V}(\mathbf{x}_1, \mathbf{x}_2)$ is the scattering potential with a (non-normalized) contrast function $m(\mathbf{x})$ compatible with the use of a general heterogeneous background media and is given by

$$\tilde{V}(\mathbf{x}_1, \mathbf{x}_2) = m(\mathbf{x}_1)\delta(\mathbf{x}_1 - \mathbf{x}_2) \quad . \quad (9)$$

Additionally, $\bar{G}^{(0)}(\mathbf{x}, \mathbf{x}')$ is the modified Green's function that incorporate the k_0^2 factor to allow for the spatial variation of the scattering potential on the remaining portion of the interaction (Kouri and Vijay, 2003) and is given by

$$\bar{G}^{(0)}(\mathbf{x}, \mathbf{x}') \equiv k_0^2 G^{(0)}(\mathbf{x}, \mathbf{x}'). \quad (10)$$

The forward problem is to determine the pressure wavefield $p(\mathbf{x})$, given a velocity model and knowledge of the source.

Discretization and implementation

In order to implement any forward modelling and inversion, a suitable model discretization has to be carried out. Hence, the solving of the forward problem can be computationally achieved by discretizing the Lippmann-Schwinger eq. (7) and Dyson eq. (8), using a discretization formulation given in Jakobsen and Ursin (2015). Since a typical acquisition geometry for a seismic survey consists of multiple sources with a given frequency band width and receivers, discretizing the data integral involves dividing the survey area into grid cells and getting discrete values for sources, receivers and frequency spectrum.

We assume that the seismic data is recorded at N_R receivers $R_i, i \in \{1, 2, ..., N_R\}$ from N_S sources $S_j, j \in \{1, 2, ..., N_S\}$. The survey area can be discretized into a set of N_V grid cells representing the positions of scattering points $x_k, k \in \{1, 2, ..., N_V\}$. Based on this discretization formulation, we can arrange the total and background wavefields at the

receiver positions (R) and scattering domain positions (V) into vectors $\mathbf{P}_R(\mathbf{P}_R^{(0)})$ and $\mathbf{P}_V(\mathbf{P}_V^{(0)})$. The discrete versions of eq. (7) become:

$$\mathbf{P}_R = \mathbf{P}_R^{(0)} + \overline{\mathbf{G}}_{RV}^{(0)}\mathbf{V}\mathbf{P}_V \quad , \tag{11}$$

$$\mathbf{P}_V = \mathbf{P}_V^{(0)} + \overline{\mathbf{G}}_{VV}^{(0)}\mathbf{V}\mathbf{P}_V \quad , \tag{12}$$

where $\mathbf{V}$ is a diagonal matrix with the scattering potential $\tilde{V}$ for a heterogeneous model at each scattering point. In a similar manner eq. (8) leads to

$$\overline{\mathbf{G}}_{RV} = \overline{\mathbf{G}}_{RV}^{(0)} + \overline{\mathbf{G}}_{RV}^{(0)}\mathbf{V}\overline{\mathbf{G}}_{VV}, \tag{13}$$

and

$$\overline{\mathbf{G}}_{VV} = \overline{\mathbf{G}}_{VV}^{(0)} + \overline{\mathbf{G}}_{RV}^{(0)}\mathbf{V}\overline{\mathbf{G}}_{VV}. \tag{14}$$

The matrices considered in eqs. (11) - (14) are source-independent and contain the modified Green's function introduced in eq. (10).

Following eq. (11), the source-dependent relations for the data and domain equations can be expressed through source-receiver Green function matrices $\mathbf{G}_{RS}^{(0)}$ and $\mathbf{G}_{RS}$ given by Jakobsen and Ursin (2015)

$$\mathbf{G}_{RS} = \mathbf{G}_{RS}^{(0)} + \overline{\mathbf{G}}_{RV}^{(0)}\mathbf{V}\mathbf{G}_{VS}, \tag{15}$$

where the corresponding matrices $\mathbf{G}_{RS}$ and $\mathbf{G}_{VS}$ as noted in eq. (12) are related by

$$\mathbf{G}_{VS} = \mathbf{G}_{VS}^{(0)} + \overline{\mathbf{G}}_{VV}^{(0)}\mathbf{V}\mathbf{G}_{VS} \quad . \tag{16}$$

The formulas in eqs. (15) and (16) are referred to as the Dyson equations for the source-receiver and source-volume Green's functions respectively (see Jakobsen and Ursin, 2015). The Dyson equations physically imply that there exists a connection between the Green's functions for the background medium and actual (heterogeneous) medium through a multiple scattering process. From eq. (16), it follows that the source-volume Green's function $\mathbf{G}_{VS}$ for the heterogeneous media is computed by matrix inversion as

$$\mathbf{G}_{VS} = (\mathbf{I} - \mathbf{V}\overline{\mathbf{G}}_{VV}^{(0)})^{-1}\mathbf{G}_{VS}^{(0)} \quad . \tag{17}$$

We consider N_f discrete frequency values $f_j = jf_0$ where f_0 is the lowest frequency of the signal and $j = 1,...,N_f$. Here, the value N_f should be chosen such that aliasing is avoided and the size of each grid cell should be chosen small compared to the dominant wavelength. Let $\delta\mathbf{d}$ be a vector containing all the different frequency components of the scattered wavefield for all sources and all receivers. Using eq. (17) in conjunction with the Dyson eq. (15) we calculate the source-receiver Green's function (for the heterogeneous background media) used for the forward modelling of the seismic data $\delta\mathbf{d}$ in the frequency domain

$$\delta\mathbf{d} \equiv (\mathbf{G}_{RS} - \mathbf{G}^{(0)}_{RS})\tilde{\mathbf{f}} = \mathbf{G}^{(0)}_{RV}\mathbf{V}\mathbf{G}_{VS}\tilde{\mathbf{f}} \quad , \tag{18}$$

where the S-dimensional vector $\tilde{\mathbf{f}}$ contains information about the seismic source distribution.

In seismic time-lapse applications, we can estimate changes in seismic response corresponding to the same strata at different time intervals. This results into time-lapse (difference) seismograms that can be used to quantitatively study the changes in the subsurface properties.

The inverse problem

The inverse problem involves finding the velocity model (scattering potential $\mathbf{V}$) based on the seismic source information and the scattered pressure wavefield $\delta\mathbf{d}$ recorded by the receivers. A promising approach that provides high quality images of the subsurface is FWI. The approach uses the full information content including travel-times, amplitudes, converted waves, and multiples of the seismic data; to find a velocity model that matches the seismic wavefield. In general, FWI finds a model $\mathbf{m}$ that generates synthetic data ($\mathbf{G}(\mathbf{m})$) that is close to observed (measured) data ($\mathbf{d}$). The inverse problem can be formulated as a least-squares optimisation problem:

$$\text{Find } \mathbf{m} \text{ such that } E(\mathbf{m}) = \left\|\mathbf{G}(\mathbf{m}) - \mathbf{d}\right\|_2^2 \text{ is minimised,} \tag{19}$$

where $E(\mathbf{m})$ is the objective function.

We solve the inverse problem using an iterative method (discussed below) based on inverse scattering theory. Iterative inversion approaches have for long been used to perform full-wave non-linear seismic inversion in order to overcome the assumptions implicit in linear inversion (see Zhang et al., 2013; Liao, 2015; Jakobsen and Ursin, 2015). This is achieved by reducing a non-linear inverse problem into a sequence of linear inverse problems. Within the inverse scattering approach, it requires that the wavefield within the scattering domain is updated after each iteration.

Distorted Born iterative T-matrix method

The distorted Born iterative T-matrix (DBIT) method, like any other method based on distorted Born iterative (DBI) approach, is motivated by expressing the field scattered by a medium relative to a heterogeneous assumed background. The underlying difference between DBIT and DBI is the use of the T-matrix for a dynamic background medium in the DBIT. This follows from combining the T-matrix approach (Jakobsen, 2012; Newton, 2013) with the distorted Born formulation. In the DBIT, the Green's functions in the background medium are updated after each iteration using the T-matrix approach. The independence of the T-matrix on the source-receiver geometry suggests that the DBIT may have great potential in time-lapse seismics. We follow the treatment given in (Jakobsen and Ursin, 2015) to deduce the formulas inherent in the DBIT inversion approach.

We begin by introducing the T-matrix perspective (Jakobsen, 2012) into the DBA. The source-independent Dyson eqs. (13) and (14) can be re-written exactly by considering the fundamental definition of the T-matrix as

$$\overline{\mathbf{G}}_{RV} = \overline{\mathbf{G}}^{(0)}_{RV} + \overline{\mathbf{G}}^{(0)}_{RV}\mathbf{T}\overline{\mathbf{G}}^{(0)}_{VV}, \tag{20}$$

$$\overline{\mathbf{G}}_{VV} = \overline{\mathbf{G}}^{(0)}_{VV} + \overline{\mathbf{G}}^{(0)}_{RV}\mathbf{T}\overline{\mathbf{G}}^{(0)}_{VV}, \tag{21}$$

where the T-matrix $\mathbf{T}$ describes all the effects of scattering (Jakobsen, 2012) and is related to the scattering potential $\mathbf{V}$ through the equation

$$\mathbf{T} = (\mathbf{I} - \mathbf{V}\overline{\mathbf{G}}^{(0)}_{VV})^{-1}\mathbf{V}. \tag{22}$$

A similar treatment can be given to the source-independent Dyson eqs. (15) and (16) such that they can be rewritten exactly as

$$\mathbf{G}_{RS} = \mathbf{G}^{(0)}_{RS} + \overline{\mathbf{G}}^{(0)}_{RV}\mathbf{T}\mathbf{G}^{(0)}_{VS}, \tag{23}$$

$$\mathbf{G}_{VS} = \mathbf{G}_{VS}^{(0)} + \overline{\mathbf{G}}_{VV}^{(0)} \mathbf{T} \mathbf{G}_{VS}^{(0)}, \tag{24}$$

The formulation above allows us to use the T-matrix to compute and update Green's functions in the background medium.

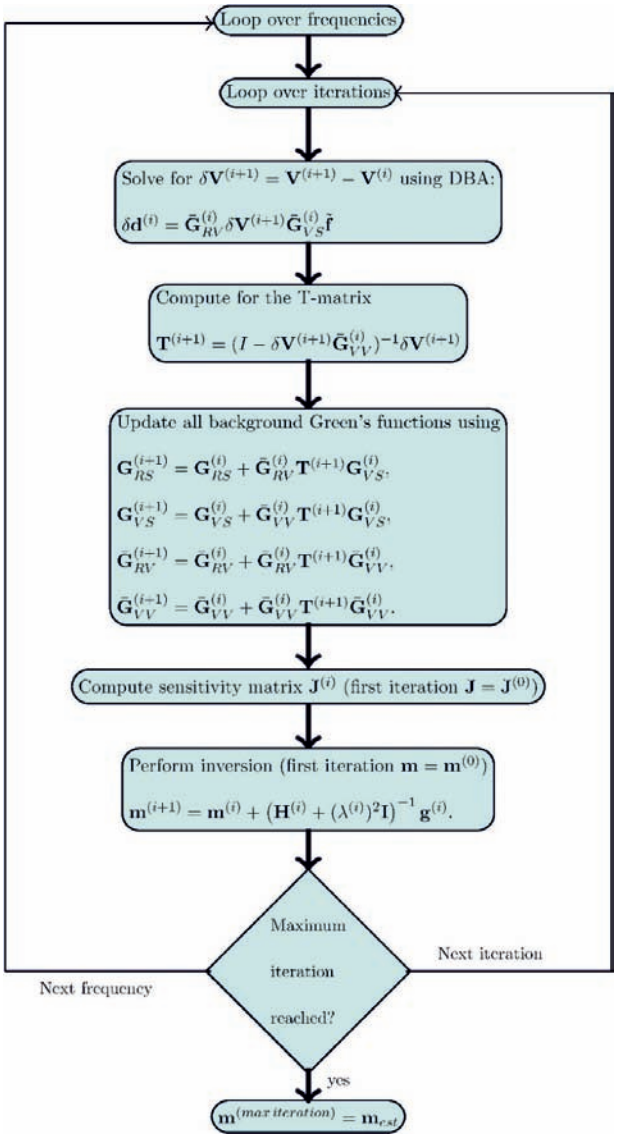

Fig. 1. The DBIT method workflow for waveform inversion.

Introducing a variation in the scattering potential $\delta\mathbf{V}$ and setting the background model to be equal to the model from the previous iteration, we can obtain a linear relation between the dynamic data residual $\delta\mathbf{d}$ for two iterations and the related variation in the scattering potential (Fig. 1). This makes it possible to avoid the inversion of a huge matrix at each iteration while introducing some approximations into the model updating procedure (Jakobsen and Ursin, 2015), and greatly reduces the computational cost. The waveform inversion is implemented in the frequency domain. Fig. 1 shows the work flow for the waveform inversion with the relevant formulas.

Details of the implementation for multiple sources and frequencies, and an explicit representation of the sensitivity matrix $\mathbf{J}^{(i)}$ in terms of Green's functions are discussed in (Jakobsen and Ursin, 2015). The inversion procedure shown in Fig. 1 reduces a non-linear inverse problem into a sequence of linear problems where the data residual vector $\delta\mathbf{d}^{(i)}$ at iteration i is

$$\delta\mathbf{d}^{(i)} = \mathbf{J}^{(i)}\delta\mathbf{m}^{(i+1)}, \tag{25}$$

where the vector $\delta\mathbf{m}^{(i+1)}$ represents the changes in all the model parameters between two successive iterations. For every grid block, the inversion process at each iteration i retrieves the components $m^{(i)}$ of the estimated model parameter vector $\mathbf{m}^{(i)}$

$$m^{(i)} = \left(\frac{\left[c^{(0)} \right]^2}{\left[c^{(i)} \right]^2} - 1 \right) \quad , \tag{26}$$

where c and $c^{(0)}$ is the estimated wave-speed within each computational grid block for the actual and reference medium. The solution for $\delta\mathbf{m}^{(i+1)}$ results from minimising a regularised objective function:

$$E(\delta\mathbf{m}^{(i+1)}) = \left\| \delta\mathbf{d}^{(i)} - \mathbf{J}^{(\mathbf{i})}\delta\mathbf{m}^{(i+1)} \right\|_2^2 \quad (\lambda^{(i)})^2 \left\| \delta\mathbf{m}^{(i+1)} \right\|_2^2 . \tag{27}$$

By constructing the Hessian matrix and gradient vector, we can use the conventional FWI notation provided in Virieux and Operto (2009) to write the model update formula that minimises the above objective function as

$$\mathbf{m}^{(i+1)} = \mathbf{m}^{(i)} + \left(\mathbf{H}^{(i)} + (\lambda^{(i)})^2\mathbf{I}\right)^{-1}\mathbf{g}^{(i)}. \quad (28)$$

In eq. (28), the vector $\mathbf{g}^{(i)}$ and matrix $\mathbf{H}^{(i)}$ represent the gradient vector and Hessian matrix at the *i*-th iteration, and are defined as (Jakobsen and Ursin, 2015)

$$\mathbf{g}^{(i)} = \Re\left[\left(\mathbf{J}^{(i)}\right)^{\dagger}\delta\mathbf{d}^{(i)}\right], \quad (29)$$

$$\mathbf{H}^{(i)} = \Re\left[\left(\mathbf{J}^{(i)}\right)^{\dagger}\mathbf{J}^{(i)}\right], \quad (30)$$

where $\mathbf{J}^{\dagger}$ is the transpose of the Jacobian matrix and $\Re$ denotes the real part of a complex number. The data residual $\delta\mathbf{d}^{(i)}$ at the *i*-th iteration is obtained by subtracting the quantity $\mathbf{J}^{(0)}\mathbf{m}^{(i)}$ from the observed scattered wavefield relative to the initial model $\delta\mathbf{d}_{obs}^{(0)}$ given as

$$\delta\mathbf{d}^{(i)} = \delta\mathbf{d}_{obs}^{(0)} - \mathbf{J}^{(0)}\mathbf{m}^{(i)}. \quad (31)$$

The regularization parameter $\lambda^{(i)}$ stabilises the solution at each iteration *i* since the inversion problem is ill-posed. In this particular inversion scheme, $\lambda^{(i)}$ at the *i*-th iteration is chosen using (Farquharson and Oldenburg, 2004)

$$\lambda^{(i)} = \max(\lambda a^{(i-1)}, \lambda^{*}), \quad (32)$$

where λ^{*} is the optimal value of the regularization obtained using the L-curve method and $0.1 < a < 0.9$ (Jakobsen and Ursin, 2015).

Time-lapse seismic inversion

Our goal is to apply FWI to time-lapse data; to invert time-lapse model changes. Hence, time-lapse inversion is a further step beyond inversion of a single survey dataset. It involves reconstructing the difference image of the subsurface between repeated survey datasets obtained at different time spans over a reservoir. Let us assume two different data sets (baseline $\mathbf{d}_{\mathrm{b}}$ and monitor $\mathbf{d}_{\mathrm{m}}$) corresponding to different time spans. We consider three inversion approaches to time-lapse seismic data, as illustrated in Fig. 2 and discussed below.

In the first approach, we perform baseline model $\mathbf{m}_b$ inversion and monitor model $\mathbf{m}_m$ inversion separately by solving eq. (19), in order to obtain corresponding estimates $\mathbf{m}_b^{est}$ and $\mathbf{m}_m^{est}$. We utilise the same starting model for the two separate inversions. The difference between the inverted baseline and inverted monitor models correspond to the time-lapse variation.

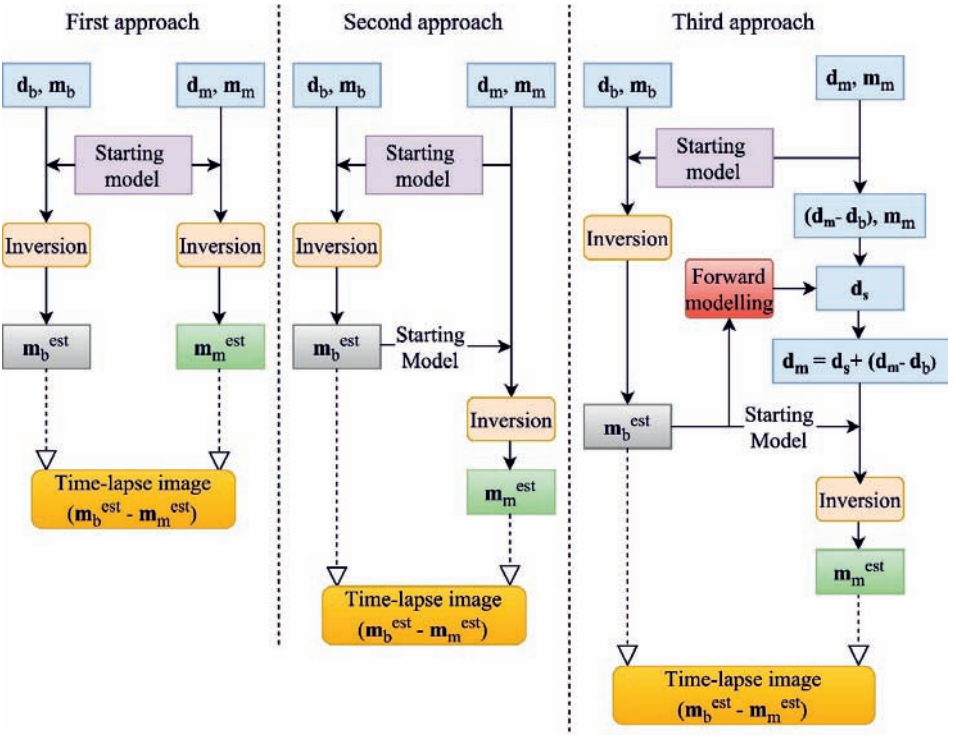

Fig. 2. A graphical illustration of the general workflow of the first, second, and third inversion approach.

In the second approach, we supply the inverted baseline model as the starting model for the monitor inversion known as the sequential difference (e.g., see Asnaashari et al., 2015). The time-lapse model is obtained by subtracting the recovered baseline from the recovered monitor model. This approach may be advantageous in that it is not affected too much by repeatability issues of the two acquisition surveys (baseline and monitor). From the implementation point of view, this approach should reduce the number of iterations needed to reconstruct the monitor model since we are starting from the baseline model. We expect that if the baseline model is

close to the monitor model (as in most time-lapse problems), the reconstruction of time-lapse changes should be improved greatly.

In the third approach, also known as double-difference strategy (Raknes et al., 2013; Zhang and Huang, 2013; Asnaashari et al., 2015), we invert for the time-lapse data variation (perturbation only). This also involves using the recovered baseline model as the starting model for the inversion of the modified monitor dataset $\bar{\mathbf{d}}_m$

$$\bar{\mathbf{d}}_m = \mathbf{d}_s + (\mathbf{d}_m - \mathbf{d}_b) \quad , \tag{33}$$

where $\mathbf{d}_s$ is the synthetic data obtained using forward modelling in the last step of the recovered baseline model, and the quantity $(\mathbf{d}_m - \mathbf{d}_b)$ is the observed time-lapse data variation. To recover the time-lapse model, we subtract from the recovered model, the recovered baseline model. The double-difference strategy is expected to reduce artefacts in the recovered time-lapse model since possible inconsistencies in the baseline inversion have less effects on the time-lapse difference data reconstruction. We compare the three approaches to establish their robustness in reconstruction of time-lapse changes.

NUMERICAL RESULTS

We examine the feasibility of distorted Born T-matrix approach for forward modelling and inversion; as a tool to monitor CO_2 injection and identify zones of CO_2 accumulation. For simplicity, we use a two-dimensional acoustic approximation in our numerical experiments. It has been shown, for example, that acoustic FWI could be used for short-offset data (Barnes and Charara, 2009), and acoustic modelling is a potential approximation for time-lapse seismic modelling at the near and middle offsets (Shahin et al., 2011; Willemsen et al., 2016).

The velocity model setup and CO_2 injection

We created a two-dimensional velocity model in vertical cross-section corresponding to the geometry shown in Fig. 3. The successive layers $\Omega_1, \Omega_2, \Omega_3, \Omega_4$ have velocities of 2200, 2500, 2400, and 2600 m/s. Red stars and blue dots in the diagram represent the source and receiver locations, respectively. The dimensions of the model are (length × depth) = 2400 m × 960 m. In order to simulate a CO_2 injection process in the model, we assume there is a single CO_2 injector at a given depth in domain Ω_3. In this feasibility experiment, our injection point is at a depth of 500 m which is

100 m below the reservoir top. Shallow CO_2 injection experiments (depth less than 1000 m) are typical for many test sites (e.g., Gritto et al., 2004; Zhang et al., 2013; Nowroozi et al., 2016). However, a larger depth of injection (greater than 1000 m) would ensure efficient utilisation of the pore spaces (since CO_2 is in its supercritical state), and would enable a longer isolation of CO_2 from the atmosphere.

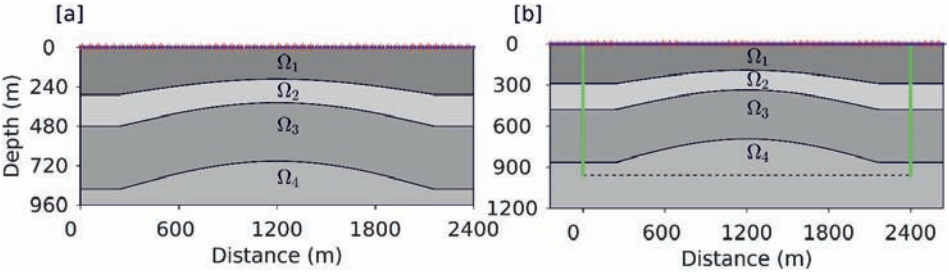

Fig. 3. Geological model geometries. (a) original model; (b) model with extended boundaries. The red stars show the positions of sources, blue dots show the positions of receivers on the surface, and the green dots show the positions of borehole receivers to the left and right edges of the original model. The black dotted line indicates the extent of the original model.

The baseline case corresponds to a model before CO_2 injection (Fig. 4a) and the monitor case (Fig. 4b) after two years of injection. We simulate the injection by a decrease in velocity values of the baseline model using a Gaussian model that simulates the injection of a fluid into a permeable reservoir layer. Although, the model has some limitations, mostly the simplified vertical distribution of the layers and unknown quantity of CO_2 injected, we obtain a reasonable picture of likely CO_2 distribution in the reservoir layer. The velocity reduction is up to 100 m/s corresponding to about 5% decrease within the reservoir region (layer Ω_3). The velocity difference between the monitor and baseline (time-lapse model) are shown in Fig. 4c.

Forward modelling of time-lapse data

We demonstrate the possibility of using distorted Born approximation eq. (8) for seismic forward modelling. The modelling parameters are shown in Table 1. We employed 50 sources, placed at intervals of 10 m from the x-locations of 12 to 2364 m, and 101 receivers equally spaced at the surface along the lateral direction from x = 0 m to x = 2400 m. Our interest is to model the time-lapse seismograms corresponding to the difference structure accruing in the earth volume due to injection of CO_2 and later reconstruct it within a non-linear inversion approach. The time-lapse synthetic data were

generated by considering the baseline model (Fig. 4a) as the reference (heterogeneous background) medium and the monitor model as perturbed medium (see Zhang, 2006), such that the scattered field is directly connected to the difference data (time-lapse data). For this case, the difference model correspond to the perturbation.

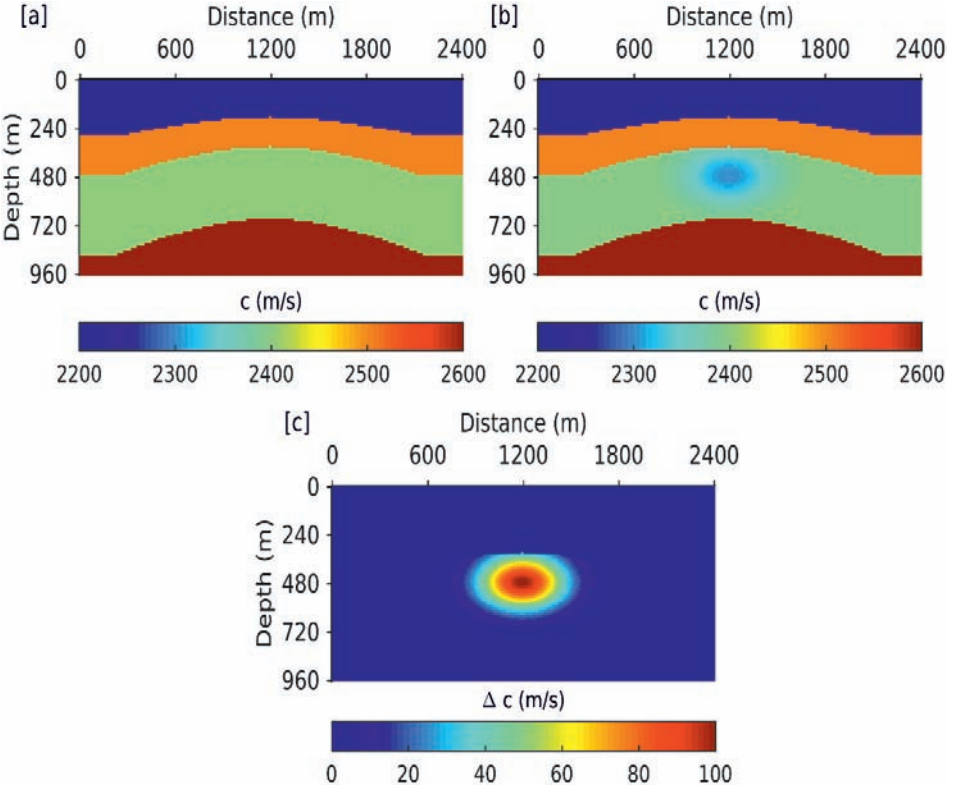

Fig. 4. Time-lapse velocity models for CO_2 monitoring: (a) baseline P-wave velocity model before injection; (b) monitor P-wave velocity model after injection; (c) time-lapse change of P-wave velocity (time-lapse model).

Table 1. Modelling parameters for the 2D model.

Number of grid-blocks	Grid size (m)	Sampling rate	Source function	Record length
x x z = 200 x 80	dz = 12 dx = 12	0.01 s	Ricker wavelet	2s

In order to make the numerical experiments more realistic, we add complex Gaussian white noise to each frequency component of clean synthetic data **d** using the formula (Jakobsen and Ursin, 2015):

$$\mathbf{d}^{noisy} = \mathbf{d} + \frac{\|\mathbf{d}\|}{\sqrt{SNR}} \frac{\mathbf{e}}{\|\mathbf{e}\|}, \tag{34}$$

where *SNR* is the signal-to-noise ratio and $\mathbf{e} = (\mathbf{e}_1 + i\mathbf{e}_2)/\sqrt{2}$ is a vector of the white noise consisting of vectors $\mathbf{e}_1$ and $\mathbf{e}_2$ of same length as **d**, having random numbers taken from the zero-mean Gaussian distribution with unit standard deviation. The scaling in eq. (34) gives us the desired *SNR*, and the selected noise-level could be interpreted as the remaining noise level after removing all the acquisition-related effects from the seismic data. For our numerical experiments, we consider a noise level of 10% corresponding with a *SNR* equal to 20 dB.

Fig. 5 shows a common shot gather for the difference data (time-lapse data) due to the changes resulting from CO_2 injection. The injection effects can be predicted in the difference sections. The effects of random noise on the seismograms are clearly manifested in the right panel of Fig. 5. The seismograms would not be visible at all with more noise added.

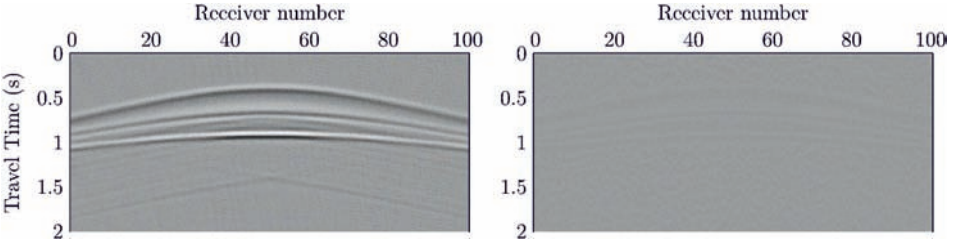

Fig. 5. Time domain synthetic shot gathers of the scattered field corresponding to the difference data for baseline and monitoring models in Fig. 4. Left panel: noise-free seismograms; Right panel: noisy difference data (*SNR* = 6 dB), the time-lapse seismic events are blinded by a high level of random noise.

To understand how well the distorted Born performs for forward modelling of time-lapse data effects, we have compared, in Fig. 6, the time-lapse seismograms calculated using the Born approximation, distorted-Born and exact T-matrix. The seismograms shown in Fig. 6 correspond to a source-receiver geometry at the surface, with a single source in the middle of the model, and 20 receivers equally distributed from $x = 0$ m to $x = 2400$ m. Important differences exist especially with the predictions of the Born approximation. The CO_2 injection model difference seismograms obtained

using the Born approximation are inaccurate and the CO_2 effects on the velocity field is not well distinguished. This demonstrates yet another inadequacy of the Born approximation in distinguishing seismically the effects of CO_2 injection on the seismic velocity field within the reservoir volume. Wrong predictions of the time-lapse time-shifts and amplitudes by the Born approximation are expected for reservoirs with large contrast volumes (Ikelle and Amundsen, 2005). Note that the spatial extension of the perturbation is large and the reservoir thickness is big. The distorted Born approximation still performs very well in predicting the time-lapse seismograms even when the thickness and depth of the reservoir increases. CO_2 accumulation effects are associated with high amplitudes in the difference seismic section. The reflectivity due to the injection process is well imaged on the seismic data.

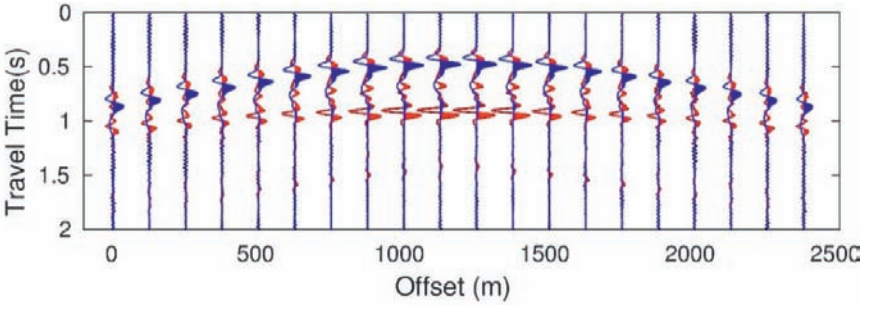

(a) Shot gather for three predictions superimposed.

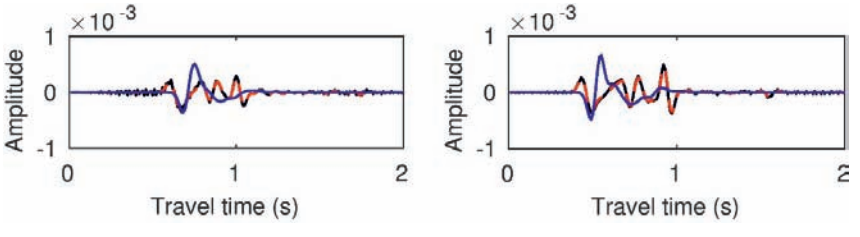

(b) Seismogram comparison at receivers 3 (left) and 14 (right).

Fig. 6. Comparison of time-lapse seismograms for the model shown in Fig. 4c as predicted by the Born approximation (blue), distorted Born (black) and exact T-matrix solution (red). The shot is located at the *x*-location of 1200 m.

Clearly, one sees that the distorted Born approximation and exact T-matrix (Jakobsen, 2012) give similar results. In the real world, the reservoir is usually thin and therefore the distorted-Born approximation can be applicable for time-lapse seismics provided the reference model is close to the monitor model. Note that the only difference between the baseline and monitor models is the time-lapse velocity change in the third layer.

Generation of synthetic seismic waveform data

We generate synthetic seismic reflection data using the T-matrix solution (Jakobsen, 2012) in the frequency domain for a selection of frequencies used in the inversion. The background medium is isotropic and homogeneous with a P-wave velocity of 2000 m/s, and the survey parameters are similar to those used in the previous example. A Ricker wavelet with central frequency 7.5 Hz as source excitation for both baseline and monitor surveys is used.

Inversion results and discussion

We apply the non-linear inversion approach of the DBIT method to noiseless data to study the robustness and behaviour of this method in reconstructing the time-lapse structural changes for the velocity models shown in Fig. 4. We investigate the possibility of using this non-linear approach to noisy data, and to test which approach may maintain relatively low levels of image artefacts and provide accurate quantitative estimates of time-lapse velocity changes.

We solve the inverse problem using the three inversion approaches mentioned earlier. The objective is to estimate the change in the velocity values after the injection period of 2 years. For both approaches, the inversion was run for six frequencies distributed uniformly over the frequency spectrum of the source signature (1, 3, 7.5, 10, 15 and 18 Hz). These frequencies were chosen based on the strategy given in Sirgue and Pratt (2004) and experience from different numerical tests. As the inversion grid, we use a different uniform grid of size 24×24 m in order to partially avoid committing an inverse crime. The inversion is performed by inverting one frequency data at a time from the lowest to the highest frequency, with a maximum of 18 iterations per frequency to minimise the error function. The regularization is achieved using Tikhonov method in conjunction with the scheme in eq. (32).

In this synthetic inversion example, the same reference velocity model shown in Fig. 7a, which is a linearly increasing velocity model, is used for the independent inversion of the baseline and monitor in the first approach. The true reference model (baseline) and monitor model are shown in Figs. 4a and 4b, respectively. Fig. 7 shows the result obtained using the first approach with two independent waveform inversions. Figs. 7c and 7e are the baseline and monitor inversion results for noise-free data. The recovered time-lapse difference model obtained using the first inversion approach is shown in Fig. 7d for noise-free data, and in Fig. 7f for noisy data. The inversion results using the first approach contain some artefacts outside the monitoring area of the reservoir as seen in Figs. 7d, even in the case of

noise-free data, and the time-lapse velocity changes are not accurately recovered for noisy data (Fig. 7f).

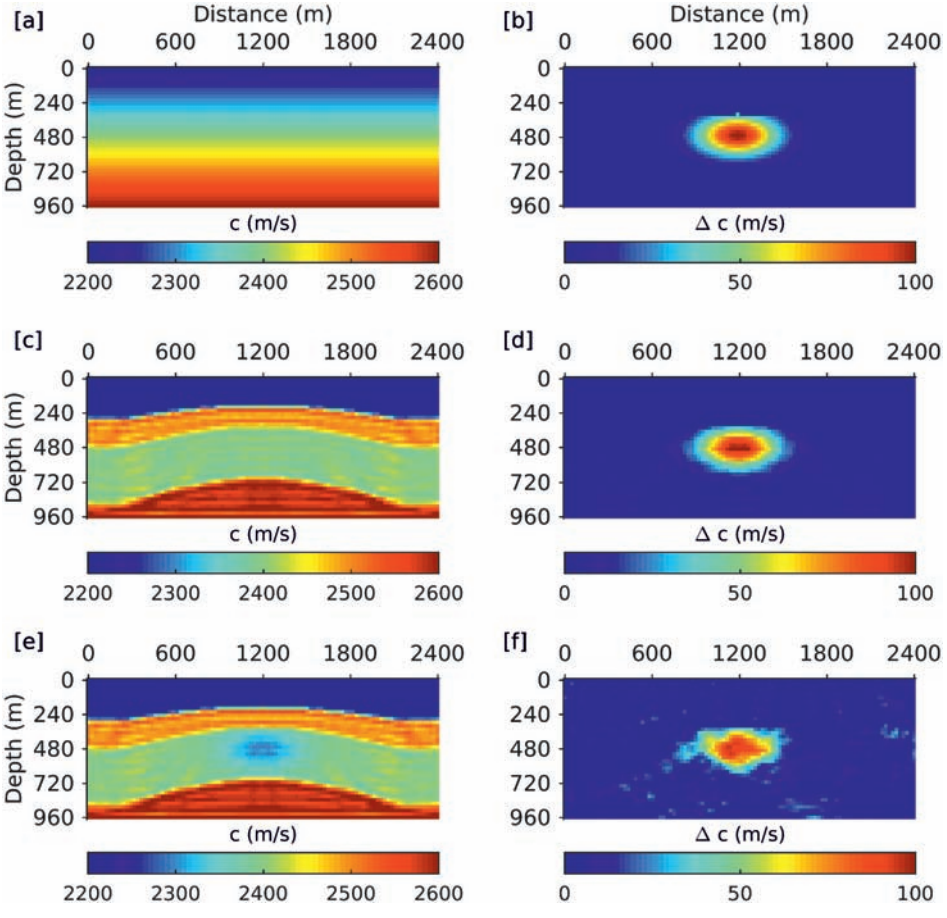

Fig. 7. Inversion of T-matrix generated data using the first approach: (a) the reference model used as starting velocity model; (b) the true time-lapse V_P model; (c) recovered baseline model; (d) recovered time-lapse V_P model (simple subtraction of the independent inversion results of baseline and monitor surveys) using noise-free data; (e) recovered monitor model; (f) recovered time-lapse V_P model using noisy data. The signal-to noise ratio is 20 dB.

The time-lapse model recovered by the inversion from second approach is shown in Figs. 8d and 8f. The starting model (Fig. 8a) for the monitor inversion is the recovered baseline model from the first approach. The second inversion approach introduces artefacts in the time-lapse image.

This could be due to the inconsistent convergence of the monitor model inversion as it tries to recover the badly reconstructed events of the starting model (the recovered baseline model). Also, differences in the modelling engine used for modelling of measurement data and inversion could result into artefacts since the time-lapse model is obtained by raw subtraction. However, the second approach ably recovers time-lapse changes in the velocities even with noisy data.

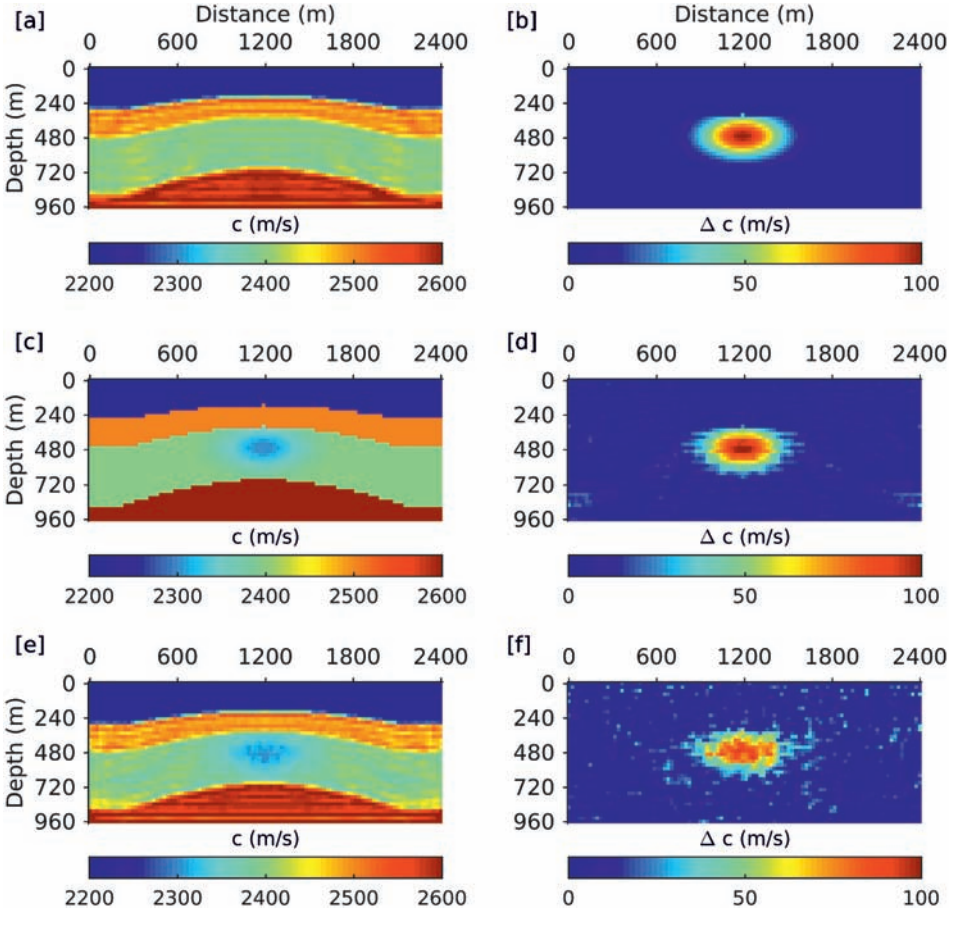

Fig. 8. Inversion of T-matrix generated data using the second approach: (a) the final recovered baseline model used as the starting velocity model; (b) recovered time-lapse V_P model starting from the true baseline model (Fig. 4a), and using same discretization grid sizes for forward modelling and inversion (inverse crime); (c) the true monitor model; (d) inversion result of time-lapse V_P model starting from the final recovered baseline model using noise-free data; (e) recovered monitor model; (f) recovered time-lapse V_P model using noisy data. The signal-to noise ratio is 20 dB.

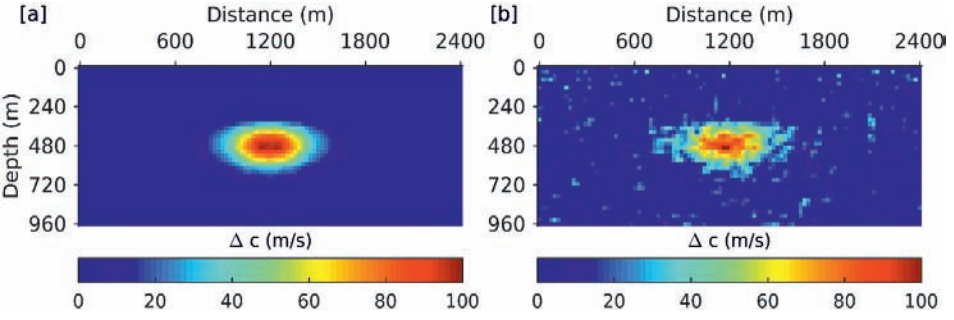

Fig. 9. Inversion of T-matrix generated data using the third approach: (a) recovered time-lapse V_P model using noise-free data; (b) recovered time-lapse V_P model using noisy data, signal-to noise ratio is 20 dB.

When using the true baseline model as the starting model for monitor inversion (Fig. 8b), the second approach gives better inversion results. This demonstrates the importance of an accurate recovered baseline model for improved reconstruction of time-lapse variations. When Figs. 8b and 8d are compared, we observe the influence of using different grid sizes for forward modelling and inversion (inverse crime) on time-lapse data reconstruction. The reconstruction has less noisy artefacts outside the monitoring zone when the same grid sizes are used. While it is important to first test an inversion method under an inverse crime, the resulting reconstructions from noise-free data, which are usually accurate should not be relied on because the method may fail when applied to real/experimental data or when noise is added.

Figs. 9a and 9b show the time-lapse model produced with the third approach, for noise-free and noisy data respectively. The velocity changes are well recovered, with minimal anomalies in the perturbation zone boundaries. The image of the reservoir in Figs. 9a and 9b is improved compared with that in Figs. 8d and 8f, because the third inversion approach focuses on the time-lapse data variation (perturbation) only.

Comparing Fig. 8f with Fig. 9b, we observe that addition of noise distorts the time-lapse inversion results in both approaches, however, we still obtain a relatively good image of the velocity changes. The noise robustness of DBIT makes it a practical time-lapse inversion method. From these numerical results, it is evident that the third approach to waveform inversion greatly improves the image of the time-lapse changes, and the magnitudes of velocity changes within the reservoir are better reconstructed than in the first and second approaches. The third approach also attenuates artefacts in the time-lapse velocity difference. Clearly, DBIT performs well

in this particular injection model, reconstructing the noise-free data with no artefacts outside the monitoring region and few artefacts for noisy data. The distribution of CO_2 is therefore well imaged after injection and the quantitative characterization can be perfectly done.

Application to a finite-element-generated data set

We applied DBIT inversion to a data set that was generated using the frequency-domain acoustic finite-element package COMSOL Multiphysics. The baseline and monitor models, the source wavelet parameters together with the background properties of the model are similar to those used in the previous examples. For the grid size, we set a minimum of 7 elements per wavelength and the basis order was set to 3. Perfect Matched Layer (PML) absorbing boundaries were employed in COMSOL to prevent reflections from the boundaries. To reduce boundary effects when using T-matrix approach, the edges of the model were extended as shown in Fig. 3b. In the region of interest, we employed sources distributed uniformly from $x = 12$ to $x = 2364$ m as in the previous example, and studied two cases:

Case 1: we used 181 receivers, 101 equally spaced from $x = 0$ to $x = 2400$ m along the lateral direction (at the surface), and 40 receiver equally spaced in the borehole from $z = 2$ to $z = 960$ m to the left and right edges of the model.

Case 2: we used 101 receivers equally spaced from $x = 0$ to $x = 2400$ m along the lateral direction (at the surface).

Fig. 10 shows a comparison of the finite-element generated data and the T-matrix data. There are differences between the two data sets. This could be explained by various reasons, namely, lack of appropriate boundary conditions in the T-matrix approach that lead to inaccurate amplitudes as a result of artificial reflections from the boundaries of the model, discretization errors due to the differences in the discretization schemes, and the fact that the T-matrix approach is based on scattering theory which requires accurate knowledge of Green's function.

Fig. 11 shows the DBIT inversion results for finite-element generated data, when the the first inversion approach is used. The inversion has recovered the general trend of V_P velocity model and the values are not drastically different from the true V_P values. However, its clear that the inverted results are not as good as those in the previous examples. We observe that the reconstruction is only improved when we use borehole receivers (case 1). In case 2, the total energy of the time-lapse perturbations is not well focussed, and velocity values have been greatly underestimated. This observation is due to the fact that down-hole receivers improves the

resolution of the images than surface seismic can provide. In general, in order to improve the accuracy of our results, there is perhaps a need to introduce an absorbing layer. This is a potential topic of study for the future.

In the DBIT inversion method, each iteration requires the solution of a forward scattering problem; thus appropriate absorbing boundary conditions might be needed to attenuate artificial unwanted edge reflections in the forward simulation. Since the current numerical example employs different forward modelling and inversion engines, these unwanted reflections introduce errors into the iterations of the inversion causing the final inversion results to contain errors.

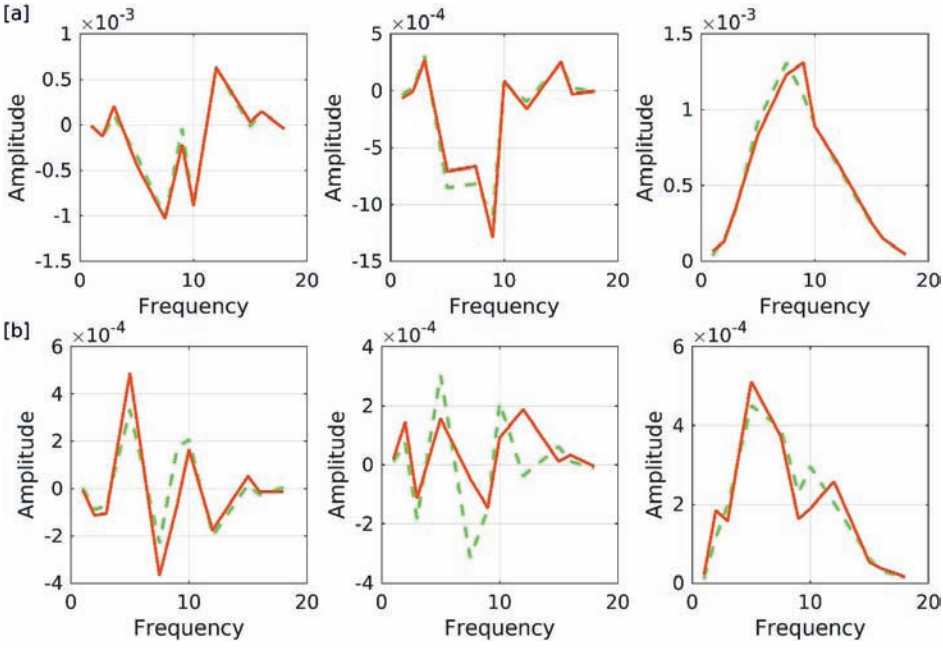

Fig. 10. Comparison between finite-element data (green) and T-matrix data (red) for the real part (Left panel), imaginary part (Middle panel) and absolute amplitude (Right panel). The shot is located at the *x*-location of 6 m for an offset: (a) 1932 m and (b) 492m.

CONCLUSIONS

In this paper, we implemented numerical modelling of seismic wave propagation using distorted Born approximation, an extension to the conventional Born method. We effectively modelled time-lapse waveforms by assuming only velocity is changed during the time-lapse acquisition and

benchmarked our results against an exact T-matrix solution. We show that with these methods in time-lapse seismics, we can easily visualise changes in waveforms between monitor survey and baseline survey by the data difference to detect variations in seismic velocities. The distorted Born performs well for our model with relatively large velocity and volume contrasts; thus improving the validity range of traditional Born approximation. The distorted Born approximation demonstrates sufficient accuracy in elucidating the CO_2 injection effects on the seismic velocities, at least for the injection model considered.

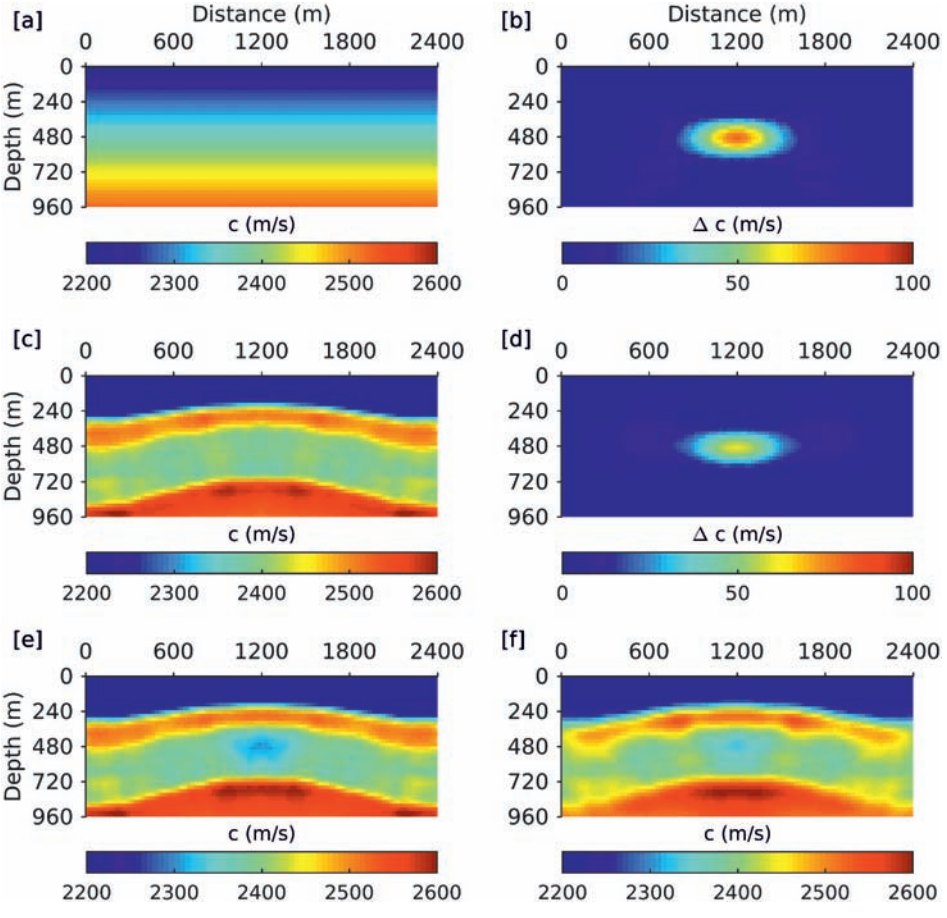

Fig. 11. Inversion of noise-free finite-element generated data using the first inversion approach: (a) the reference model used as starting velocity model; (b) recovered time-lapse V_P model for case 1; (c) recovered baseline model for case 1; (d) recovered time-lapse V_P model for case 2; (e) recovered monitor model for case 1; (f) recovered monitor model for case 2.

We also discussed and implemented the non-linear distorted Born iterative T-matrix (DBIT) inversion method that utilises the T-matrix approach from quantum scattering theory. The performance of the method was demonstrated using a 2D CO_2 injection model. The method performs well for the CO_2 injection model and we are able to obtain good inversion results at a lower computational cost–using a small number of frequencies spanning the source spectrum. We at least expect the DBIT method to be potentially useful in seismic monitoring of CO_2 sequestration and in modelling time-lapse models with relative large velocity contrasts. The resolution of the reconstructed images seems to depend directly on the ability to recover the high frequency content of the seismic data; and the accuracy of the reconstructions, on the time-lapse inversion approach selected.

Full-waveform inversion methods are normally limited to low frequencies but time-lapse variations are normally characterised as high-frequency details in the model. This may be affecting our results but still, we are able to obtain high resolution images with surprisingly fewer frequencies we used in our inversion. It would be interesting to assess the method against real data and in the absence of low frequency data; and to assess the computation time cost in details. Since DBIT considers all multiple scattering effects, its application to real data, would only require preserving true amplitudes of the data during during processing, before it can be implemented on it.

Our current implementation of the inversion scheme does not use explicit boundary conditions. One of the main factors influencing the accuracy of the seismic modelling and inversion simulation can potentially be the boundary condition used to remove edge reflections generated at the finite boundaries. Implementing absorbing boundary conditions in the T-matrix approach may be necessary to have modelling and inversion algorithms free from edge reflections. Additionally, using smaller grid blocks in the T-matrix approach would eliminate most errors related to discretization; however, limits can be imposed by computational capabilities. From the practical point of view, it would be important to understand how much injected CO_2 can be detected by the proposed methodology. Next steps will potentially include the use of Born approximations in a context of Bayesian inversion (Kaipio and Somersalo, 2006; Eikrem et al., 2016, 2017).

ACKNOWLEDGEMENTS

This work has been supported by the strategic funding of the University of Eastern Finland and by the academy of Finland (project 250215, Finnish Centre of Excellence in Inverse Problems Research).

REFERENCES

Asnaashari, A., Brossier, R., Garambois, S., Audebert, F., Thore, P. and Virieux, J., 2015. Time-lapse seismic imaging using regularized fullwaveform inversion with a prior model: which strategy? Geophys. Prosp., 63: 78-98.

Ayeni, G. and Biondi, B., 2010. Target-oriented joint least-squares migration/inversion of time-lapse seismic data sets. Geophysics, 75: R61-R73.

Ayeni, G. and Biondi, B., 2011. Wave-equation inversion of time-lapse seismic data sets. Expanded Abstr., 81st Ann. Internat. SEG Mtg., San Antonio.

Barnes, C. and Charara, M., 2009. The domain of applicability of acoustic full-waveform inversion for marine seismic data. Geophysics., 74: WCC91-WCC103.

Carcione, J.M., Picotti, S., Gei, D. and Rossi, G., 2006. Physics and seismic modeling for monitoring CO_2 storage. Pure Appl. Geophys, 163: 175-207.

Cerveny, V., 2005. Seismic Ray Theory. Cambridge University Press, Cambridge.

Chadwick, R., Noy, D., Arts, R. and Eiken, O., 2009. Latest time-lapse seismic data from sleipner yield new insights into CO_2 plume development. Energy Proced., 1: 2103-2110.

Cohen, J.K. and Bleistein, N., 1977. An inverse method for determining small variations in propagation speed. SIAM J. Appl. Mathemat., 32: 784-799.

Colton, D. and Kress, R., 2012. Inverse Acoustic and Electromagnetic Scattering Theory. Springer Science & Business Media, 93.

Couëslan, M.L., Smith, V., El-Kaseeh, G., Gilbert, J., Preece, N., Zhang, L. and Gulati, J., 2014. Development and implementation of a seismic characterization and CO_2 monitoring program for the Illinois basin–Decatur project: Greenhouse Gases. Sci. Technol., 4: 626-644.

Eikrem, K., Jakobsen, M. and Nævdal, G., 2017. Bayesian inversion of time-lapse seismic waveform data using an integral equation method. Abstracts, IOR 2017-19th Europ. Symp. Improv. Oil Recov.

Eikrem, K.S., Nævdal, G., Jakobsen, M. and Chen, Y., 2016. Bayesian estimation of reservoir properties: effects of uncertainty quantification of 4D seismic data. Computat. Geosci., 20: 1211-1229.

Farquharson, C.G. and Oldenburg, D.W., 2004. A comparison of automatic techniques for estimating the regularization parameter in non-linear inverse problems. Geophys. J. Internat., 156: 411-425.

Gritto, R., Daley, T.M. and Myer, L.R., 2004. Joint cross-well and single-well seismic studies of CO_2 injection in an oil reservoir. Geophys. Prosp., 52: 323-339.

Haffinger, P., Gisolf, A. and van den Berg, P., 2013. Towards high resolution quantitative subsurface models by full waveform inversion. Geophys. J. Internat., 193: 788-797.

Ikelle, L.T. and Amundsen, L., 2005. Introduction to Petroleum Seismology. SEG, Tulsa, OK.

Innanen, K.A., Naghizadeh, M. and Kaplan, S.T., 2014. Perturbation methods for two special cases of the time-lapse seismic inverse problem. Geophys. Prosp., 62: 453-474.

IPCC, 2014. Climate Change 2014 - impacts, adaptation and vulnerability. Regional Aspects. Cambridge University Press, Cambridge.

Ivandic, M., Juhlin, C., Lüth, S., Bergmann, P., Kashubin, A., Sopher, D., Ivanova, A., Baumann, G. and Henninges, J., 2015. Geophysical monitoring at the Ketzin pilot site for CO_2 storage: New insights into the plume evolution. Internat. J. Greenh. Gas Contr., 32: 90-105.

Jakobsen, M., 2012. T-matrix approach to seismic forward modelling in the acoustic approximation. Studia Geophys. Geodaet., 56: 1-20.

Jakobsen, M. and Ursin, B., 2015. Full waveform inversion in the frequency domain using direct iterative T-matrix methods. J. Geophys. Engineer., 12: 400.

Kaipio, J. and Somersalo, E., 2006. Statistical and Computational Inverse Problems. Springer Science & Business Media, 160.

Kasahara, J. and Hasada, Y., 2016. Time Lapse Approach to Monitoring Oil, Gas, and CO_2 Storage by Seismic Methods. Elsevier Science, Amsterdam.

Kim, Y., Cho, H., Min, D.-J. and Shin, C., 2011. Comparison of frequency-selection strategies for 2D frequency-domain acoustic waveform inversion. Pure Appl. Geophys., 168: 1715-1727.

Kirchner, A. and Shapiro, S.A., 2001. Fast repeat-modelling of time-lapse seismograms. Geophys. Prosp., 49: 557-569.

Kouri, D.J. and Vijay, A., 2003. Inverse scattering theory: Renormalization of the Lippmann-Schwinger equation for acoustic scattering in one dimension. Phys. Rev. E, 67: 046614.

Lähivaara, T., Dudley Ward, N., Huttunen, T., Rawlinson, Z. and Kaipio, J., 2015. Estimation of aquifer dimensions from passive seismic signals in the presence of material and source uncertainties. Geophys. J. Internat., 200: 1662-1675.

Liao, W., 2015. An adjoint-based Jacobi-type iterative method for elastic full waveform inversion problem. Appl. Mathemat. Computat., 267: 56-70.

Maharramov, M. and Biondi, B., 2014. Robust joint full-waveform inversion of time-lapse seismic data sets with total-variation regularization. arXiv: 1408.0645.

Marston, P.M., 2013. Pressure profiles for CO_2-EOR and CCS: Implications for regulatory frameworks: Greenhouse Gases. Sci. Technol., 3: 165-168.

Moser, T.J., 2012. Review of ray-Born forward modeling for migration and diffraction analysis. Studia Geophys. Geodaet., 56: 411-432.

Newton, R.G., 2013. Scattering Theory of Waves and Particles. Springer Science & Business Media.

Nowroozi, D., Lawton, D.C. and Khaniani, H., 2016. A framework for full waveform modeling and imaging for CO_2 injection at the FRS project. Abstracts, GeoConvention 2016.

Pevzner, R., Urosevic, M., Popik, D., Shulakova, V., Tertyshnikov, K., Caspari, E., Correa, J., Dance, T., Kepic, A. and Glubokovskikh, S., 2017. 4D surface seismic tracks small supercritical CO_2 injection into the subsurface: CO2CRC Otway project. Internat. J. Greenh. Gas Contr., 63: 150-157.

Pratt, R.G., 1999. Seismic waveform inversion in the frequency domain, Part 1: Theory and verification in a physical scale model. Geophysics, 64: 888-901.

Prieux, V., Operto, S., Brossier, R. and Virieux, J., 2009. Application of acoustic full waveform inversion to the synthetic Valhall velocity model. Expanded Abstr., 79th Ann. Internat. SEG Mtg., Houston.

Queißer, M. and Singh, S.C., 2013. Full waveform inversion in the time lapse mode applied to CO_2 storage at Sleipner: Geophys. Prosp., 61: 537-555.

Raknes, E.B., Weibull, W. and Arntsen, B., 2013. Time-lapse full waveform inversion: Synthetic and real data examples. Expanded Abstr., 83rd Ann. Internat. SEG Mtg., Houston.

Raknes, E.B., Weibull, W. and Arntsen, B., 2015. Seismic imaging of the carbon dioxide gas cloud at Sleipner using 3D elastic time-lapse full waveform inversion. Internat. J. Greenh. Gas Contr., 42: 26-45.

Romdhane, A. and Querendez, E., 2014. CO_2 characterization at the sleipner field with full waveform inversion: Application to synthetic and real data. Energy Proced., 63: 4358-4365.

Shahin, A., Stoffa, P.L., Tatham, R.H. and Seif, R., 2011. Accuracy required in seismic modeling to detect production-induced time-lapse signatures. Expanded Abstr., 81st Ann. Internat. SEG Mtg., San Antonio.

Sheen, D.H., Tuncay, K., Baag, C.E. and Ortoleva, P.J., 2006. Time domain Gauss-Newton seismic waveform inversion in elastic media. Geophys. J. Internat., 167: 1373-1384.

Shi, J.-Q., Xue, Z. and Durucan, S., 2007. Seismic monitoring and modelling of supercritical CO_2 injection into a water-saturated sandstone: Interpretation of P-wave velocity data. Internat. J. Greenh. Gas Contr., 1: 473-480.

Sirgue, L. and Pratt, R.G., 2004. Efficient waveform inversion and imaging: A strategy for selecting temporal frequencies. Geophysics, 69: 231-248.

Tarantola, A., 1984. Inversion of seismic reflection data in the acoustic approximation. Geophysics, 49: 1259-1266.

Thierry, P., Operto, S. and Lambaré, G., 1998. Fast 2-D ray+Born migration/inversion in complex media. Geophysics, 64: 162-181.

Virieux, J. and Operto, S., 2009. An overview of full-waveform inversion in exploration geophysics. Geophysics, 74: WCC1-WCC26.

White, D., 2011. Geophysical monitoring of the Weyburn CO_2 flood: Results during 10 years of injection. Energy Proced., 4: 3628-3635.

Willemsen, B., Cao, J. and Roy, B., 2016. The impact of the acoustic approximation on time-lapse FWI. Expanded Abstr., 86th Ann. Internat. SEG Mtg., Dallas: 5435-5440.

Zhang, F., Juhlin, C., Ivandic, M. and Lüth, S., 2013. Application of seismic full waveform inversion to monitor CO_2 injection: Modelling and a real data example from the Ketzin site, Germany. Geophys. Prosp., 61: 284-299.

Zhang, F., Juhlin, C., Niemi, A., Huang, F. and Bensabat, J., 2016. A feasibility and efficiency study of seismic waveform inversion for time-lapse monitoring of onshore CO_2 geological storage sites using reflection seismic acquisition geometries. Internat. J. Greenh. Gas Contr., 48: 134-141.

Zhang, H., 2006. Direct Non-linear Acoustic and Elastic Inversion: Towards fundamentally new comprehensive and realistic target identification. Ph.D. thesis, University of Houston.

Zhang, Z. and Huang, L., 2013. Double-difference elastic-waveform inversion with prior information for time-lapse monitoring. Geophysics, 78: R259-R273.